ACS Catalysis

Research Article

pubs.acs.org/acscatalysis

Electron–Hole Recombination Controlled by Metal Doping Sites in $NaTaO_3$ Photocatalysts

Longjie An and Hiroshi Onishi*

Department of Chemistry, School of Science, Kobe University, Nada, Kobe, Hyogo 657-8501 Japan

ABSTRACT: In this research, sodium tantalate ($NaTaO_3$) photocatalyst was doped with Sr^{2+} cations via solid-state or hydrothermal reactions. $NaTaO_3$–$SrSr_{1/3}Ta_{2/3}O_3$ solid solutions that had been doped through the solid-state reaction with a Sr-rich shell covering a Sr-poor core appeared. The lattice mismatch at the heteroepitaxial core–shell interface induced surface reconstruction with regularly separated steps. The steady-state population of electrons excited with Hg–Xe lamp irradiation increased by up to 180 times in the solid-solution photocatalysts in which A sites and B sites of the perovskite-structured lattice were doped with Sr^{2+}. On the other hand, A sites were selectively doped with the same cations through the hydrothermal reaction. Surface reconstruction and an enhanced electron population were absent in the A-site-doped photocatalysts. Compatible results were obtained by doping with Ca or Ba instead of Sr. Tuning of doping sites was essential to restricting recombination in $NaTaO_3$ photocatalysts doped with the alkaline-earth metals.

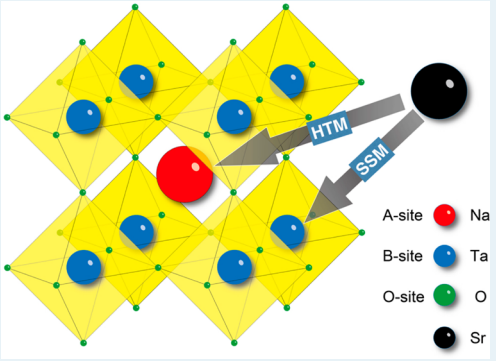

KEYWORDS: *photocatalysis, reaction kinetics, recombination, doping, solid solution, perovskite structure, surface reconstruction, solar hydrogen*

1. INTRODUCTION

Photocatalytic splitting reaction of water is one of the promising processes for production of hydrogen fuel. The photocatalysts lanthanum-doped sodium tantalate ($NaTaO_3$)[1,2] and zinc-doped Ga_2O_3[3] have the highest quantum efficiencies for water splitting. Compatible activities have also been achieved by using $NaTaO_3$ doped with the alkaline-earth metals Ca, Sr, and Ba.[4,5] In these examples, doping with heterometals is the key to efficient production of hydrogen fuel. Our earlier studies[6,7] using time-resolved infrared (IR) absorption revealed that favorable metal doping of $NaTaO_3$ restricted electron–hole recombination and thus enhanced quantum efficiency. Specific metal elements, despite being impurities in the host lattice, restrict recombination, but the mechanisms behind this restriction are still unknown. In this study, we showed that Sr^{2+} cations restricted electron–hole recombination and increased the steady-state population of photoexcited electrons by up to 180 times when we used them to dope A sites and B sites in perovskite-structured $NaTaO_3$. The same element failed to restrict recombination when it was used to dope A sites alone. Compatible results were obtained with the other alkaline-earth metals Ca and Ba. Doping B-site cations was critical to restricting recombination in $NaTaO_3$ photocatalysts.

2. EXPERIMENTAL SECTION

2.1. Photocatalyst Preparation. Strontium-doped $NaTaO_3$ photocatalysts were prepared via two methods. In the solid-state method (SSM), mixtures of Na_2CO_3 (99.8%, Kanto), Ta_2O_5 (99.99%, Rare Metallic), and $SrCO_3$ (99.9%, Kanto) were calcined in an alumina crucible at 1173 K for 1 h and then at 1423 K for 10 h.[4,5] The Na/Ta molar ratio in the mixtures was adjusted to 1.05 to compensate for Na loss during calcination. Excess Na remaining in the calcined products was washed out with water. In the hydrothermal method (HTM), 4 mol L^{-1} aqueous solutions of NaOH (96%, Wako) containing Ta_2O_5 and $SrCO_3$ were sealed in a Teflon container and then heated at 433 K for 24 h in an autoclave (OMlab-Tech, MR28).[8−10] The starting solutions had a Na/Ta molar ratio of 4. Calcium-, barium-, and potassium-doped photocatalysts were similarly prepared via SSM or HTM using $CaCO_3$ (99.5%, Wako), $BaCO_3$ (99.99%, Wako), and K_2CO_3 (99.5%, Wako), respectively, instead of $SrCO_3$. $NaTaO_3$ doped with a metal element, M, is hereafter referred to as M-NTO (SSM) when it was prepared through SSM, and as M-NTO (HTM) when it was prepared through HTM.

2.2. Photocatalyst Characterization. Doping-metal concentrations were quantified relative to the number of host Ta cations by using an energy-dispersed X-ray fluorescence (EDX) spectrometer (Shimadzu, EDX-720). The crystallographic phase was determined by using an X-ray diffractometer (Rigaku, SmartLab). The size and shape of the photocatalyst particles were observed under a scanning electron microscope (Hitachi High-Technologies, S-4800). Ultraviolet–visible (UV–vis) diffuse-reflection spectra were obtained by using a spectrometer (Jasco, V-570) with an integration sphere.

Received: July 24, 2014
Revised: April 12, 2015
Published: April 24, 2015

DOI: 10.1021/acscatal.5b00484
ACS Catal. 2015, 5, 3196–3206

Photocatalysts were fixed on Ir foil and analyzed by X-ray photoelectron spectroscopy (XPS) using a spectrometer (Ulvac-Phi, PHI X-tool) with an Al Kα excitation source. For Raman and IR measurements, each photocatalyst was suspended in water, placed on a 1-mm-thick CaF_2 plate, and then dried at 293 K for 20 h. The Raman spectrometer, which was fabricated in-house, had a He−Cd laser light source (Kimmon, IK4401R-D), grating spectrometer (Horiba Jobin Yvon, iHR320), and charge-coupled device detector (Andor, DU440BU). Excitation light with a 442 nm wavelength was focused on the photocatalyst-covered plate that was exposed to air. The power and spot diameter of the excitation light were 60 mW and 3 mm, respectively. IR absorption spectra were obtained by using a Fourier transform spectrometer (Jasco, FT/IR610). The photocatalyst-covered CaF_2 plate was placed in a vacuum of 10 Pa. Absorbance spectra with and without UV light irradiation were recorded. A Hg−Xe lamp (San-ei Electric, UVS-204S) was used as a UV light source. Light power at wavelengths of 370 nm or shorter was 60 mW cm^{-2} in the full spectrum of irradiation.

3. RESULTS AND DISCUSSION

3.1. Sr-NTO (SSM). Strontium-doped $NaTaO_3$ photocatalysts with Sr concentrations of 0.01, 0.1, 0.2, 0.3, 0.5, 0.7, 0.9, 1.8, 4.7, 7.7, 18.7, and 43.5 mol % were prepared by SSM. The perovskite phase of the photocatalysts was checked and confirmed through X-ray diffraction (XRD), as shown in Figure 1A. No impurity phase appeared. Diffraction angles and relative peak intensities of pristine $NaTaO_3$, NTO (SSM), were identical to those reported previously.[11] Diffraction peaks at Sr concentrations of 0.9 mol % or larger broadened and shifted to lower angles, as evident in Figure 1B, which features 32° peaks. The low-angle shifts indicate perovskite lattice expansion upon doping.

Two Sr-containing, perovskite-structured tantalates, $SrSr_{1/3}Ta_{2/3}O_3$ and $SrSr_{2/5}Ta_{3/5}O_{2.9}$, are known; structures of these compounds have been solved.[12,13] In the former compound, Sr^{2+} cations fully occupy A sites in the perovskite lattice, whereas Sr^{2+} with rock-salt-like ordering of TaO_6 and $(Sr_{2/3}Ta_{1/3})O_6$ octahedra substitute for one-third of the Ta^{5+} cations at the B sites.[12] In the latter, two-fifths of the B-site Ta^{5+} cations are replaced by Sr^{2+} with rock-salt-like ordering of TaO_6 and $(Sr_{4/5}Ta_{1/5})O_6$ octahedra.[13] Oxygen anion vacancies are introduced to balance the cationic and anionic charges when required in the latter compound. In the present study, $SrSr_{1/3}Ta_{2/3}O_3$ was synthesized via SSM and compared with Sr-NTO (SSM).

A mixture of $SrCO_3$, Ta_2O_5, and Na_2CO_3 was calcined and washed in a manner similar to the preparation of Sr-NTO. The Sr/Ta and Na/Ta molar ratios in the mixture were 2 and 1, respectively. EDX analysis revealed a Sr/Ta molar ratio of 1.78. The diffraction pattern of the product, which is shown in Figure 1A, was identical to the reported pattern of $SrSr_{1/3}Ta_{2/3}O_3$.[12] Peaks assignable to $NaTaO_3$ were unrecognizable, even though the starting material included $NaCO_3$. When a mixture of only $SrCO_3$ and Ta_2O_5 was calcined, the product included complex oxides in addition to $SrSr_{1/3}Ta_{2/3}O_3$. Sodium in the starting material provided nucleation centers for the perovskite framework. Thus, $NaTaO_3$ might have formed and then converted into $SrSr_{1/3}Ta_{2/3}O_3$.

The diffraction patterns of Sr-NTO (SSM) and $SrSr_{1/3}Ta_{2/3}O_3$ were qualitatively identical, as the perovskite structure is common in the two materials. Each diffraction peak

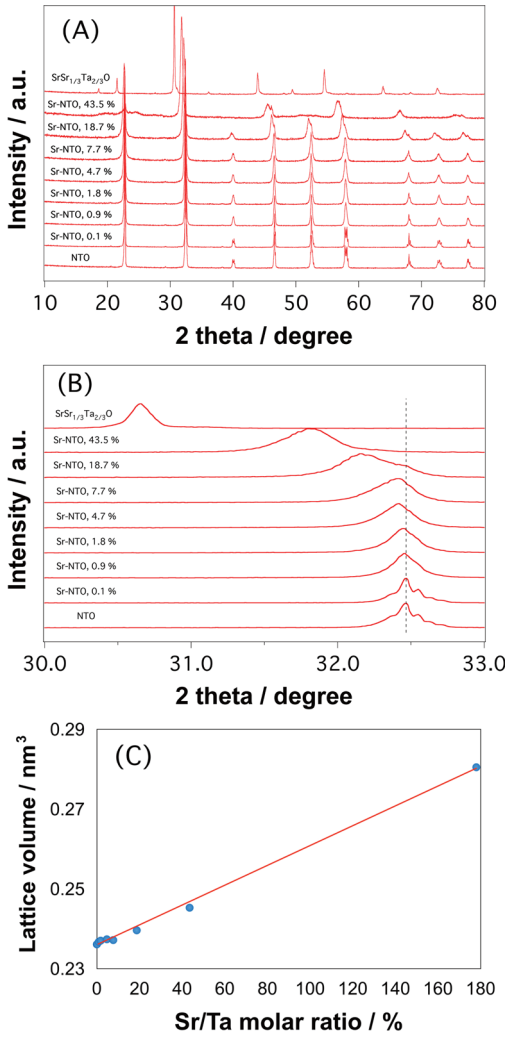

Figure 1. XRD patterns of tantalate photocatalysts with different Sr concentrations and $SrSr_{1/3}Ta_{2/3}O_3$ prepared through SSM. (A) Whole patterns, (B) shifts of 32° peaks, and (C) lattice volume as a function of Sr concentration.

of Sr-NTO (SSM) shifted to lower angles and approached the corresponding peak of $SrSr_{1/3}Ta_{2/3}O_3$ as the Sr concentration increased. The observed continuous shifts suggest solid solutions of $NaTaO_3$ and $SrSr_{1/3}Ta_{2/3}O_3$ in Sr-NTO (SSM). Preparing a solid solution of the two compounds is the easiest way to maintain the balance of cationic and anionic charges in Sr-NTO without producing a need for anion vacancies. The low-angle shifts are consistent with doping Ta^{5+} with Sr^{2+} that was required in the solid solutions. The ionic radii of 6-fold-coordinated Ta^{5+} and Sr^{2+} are 0.06 and 0.12 nm, respectively.[14] The contribution of A-site doping should be minor to lattice expansion, since the radii of 12-fold-coordinated Na^+ and Sr^{2+} cations are identical (0.14 nm).[14] The lattice volume of Sr-NTO (SSM) was determined from the diffraction results and is plotted in Figure 1C as a function of the Sr/Ta molar ratio. A straight line is fitted to the observed volumes in the full range from pristine $NaTaO_3$ (Sr/Ta = 0) to $SrSr_{1/3}Ta_{2/3}O_3$ (Sr/Ta = 1.78). The linear relation between lattice volume and Sr concentration provides good evidence for the proposed solid solutions.

In the preceding paragraph, we proposed and revealed evidence for $NaTaO_3$−$SrSr_{1/3}Ta_{2/3}O_3$ solid solutions in Sr-

DOI: 10.1021/acscatal.5b00484
ACS Catal. 2015, 5, 3196−3206

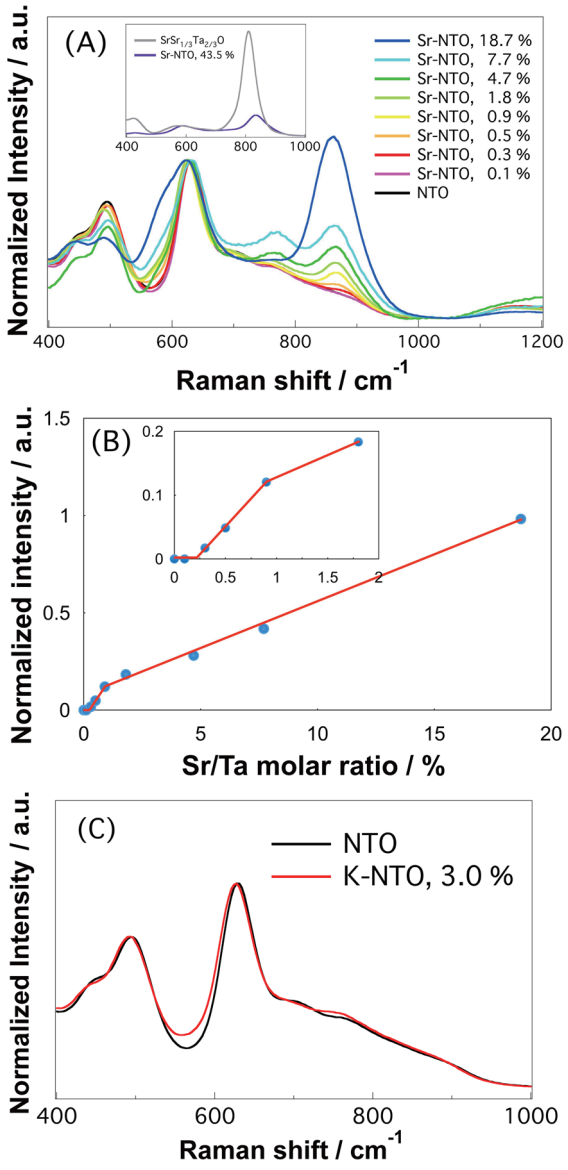

Figure 2. Raman spectra of $NaTaO_3$ photocatalysts and related materials prepared through SSM. (A) Sr-NTO (SSM) and $SrSr_{1/3}Ta_{2/3}O_3$. (B) Relative intensity of the 860 cm^{-1} band of Sr-NTO (SSM) as a function of Sr concentration. (C) The spectrum of K-NTO (SSM) compared with that of NTO (SSM).

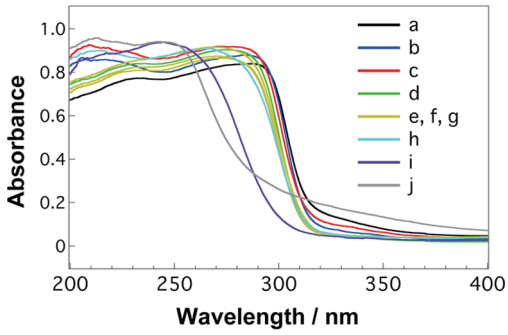

Figure 3. UV−vis diffuse-reflection spectra of Sr-NTO (SSM) doped at a, 0; b, 0.1; c, 0.3; d, 0.5; e, 0.9; f, 1.8; g, 4.7; h, 18.7; and i, 43.5 mol % and with j, $SrSr_{1/3}Ta_{2/3}O_3$. The apparent absorbance without Kubelka−Munk transformation is shown.

NTO (SSM). However, researchers,[4,5,15,16] including ourselves,[6,7] assumed simple A-site substitution in $NaTaO_3$ doped with Sr, Ca, or Ba because the 12-fold coordinated ionic radii of the metal elements are, by coincidence, similar: 0.13 (Ca^{2+}), 0.14 (Sr^{2+}), 0.16 (Ba^{2+}), and 0.14 nm (Na^{+}).[14] When the solid solutions appeared in Sr-NTO (SSM), the A and B sites were doped together despite the difference between Ta^{5+} and Sr^{2+} radii. Additional evidence for B-site doping in Sr-NTO (SSM) was obtained by Raman spectroscopy.

Figure 2A shows the Raman spectra of Sr-NTO (SSM). NTO (SSM) produced major bands at 450, 500, and 620 cm^{-1}, similar to results reported in the literature.[17] Upon Sr doping via SSM, two additional bands appeared at 860 and 760 cm^{-1}. These bands are assigned to breathing vibrations of BO_6 octahedra in B-site substituted perovskites, $AB_{1-x}B'_xO_3$. The BO_6 breathing mode, which possesses A_{1g} symmetry, cannot contribute to Raman scattering in an ideal cubic perovskite ABO_3 because of symmetry restriction. Partial replacement of B-site cations with nonequivalent B′ cations breaks down this restriction. In a number of $AB_{1-x}B'_xO_3$ perovskites, the breathing vibration produces strong Raman bands in the range of 780−850 cm^{-1}.[18−20] Indeed, $SrSr_{1/3}Ta_{2/3}O_3$ prepared in this study produced an intense band at 810 cm^{-1}, as shown in the inset of Figure 2A. The 860 cm^{-1} band of Sr-NTO strengthened with Sr concentration and merged with the 810 cm^{-1} band in $SrSr_{1/3}Ta_{2/3}O_3$. The presence of the band at 860 cm^{-1} is therefore an indication of B-site doping in Sr-NTO (SSM).

The 860 cm^{-1} band is sharp and well separated from the other Raman bands. Sensitive and quantitative detection of B-site doping is thus possible by tracing the intensity of the 860 cm^{-1} band. The intensity relative to that of the 620 cm^{-1} band is plotted in Figure 2B as a function of the Sr concentration. The 860 cm^{-1} band was not recognized on Sr-NTO (SSM) of 0.1 mol %. Upon doping at 0.3 mol % or more, the 860 cm^{-1} band appeared and strengthened linearly with concentration. A threshold for B-site doping at ∼0.3 mol % was thus evident.

Strontium cations must have occupied only A sites at concentrations below the threshold to be silent in Raman scattering. To verify this interpretation, we prepared A-site-doped $NaTaO_3$ (K-NTO (SSM)) with a potassium concentration of 3.0 mol %. Potassium cations occupied the A site,[21−23] and the 860 cm^{-1} band was absent in the spectrum in Figure 2C, as expected. The Raman results demonstrate two different types of Sr doping in $NaTaO_3$ prepared through SSM: selective doping of A sites below the threshold concentration and simultaneous doping of A and B sites above the threshold.

The reasons for Sr occupation to switch from A sites to B sites are unknown. A simulation study of La-doped $NaTaO_3$ found that the formation energy of La doping at A sites and at B sites is sensitive to La concentration.[24] A-site doping was favorable at the low-concentration extreme. Lanthanum at A sites donate electrons, and the Fermi level shifts toward the conduction band (CB) minimum. The shifted Fermi level favors the behavior of La as acceptors at B-sites. This scheme may possibly be applied to Sr-NTO. $NaTaO_3$−$SrSr_{1/3}Ta_{2/3}O_3$ solid solutions should be simulated in a future study to derive conclusions.

The electronic structure of Sr-NTO (SSM) is sensitive to the two different types of doping. The CB is derived from Ta 5d orbitals[24−26] to render it susceptible to B-site doping. Figure 3 presents UV−vis diffuse-reflection spectra of Sr-NTO (SSM) and $SrSr_{1/3}Ta_{2/3}O_3$. The middle wavelength of the absorption

DOI: 10.1021/acscatal.5b00484
ACS Catal. 2015, 5, 3196−3206

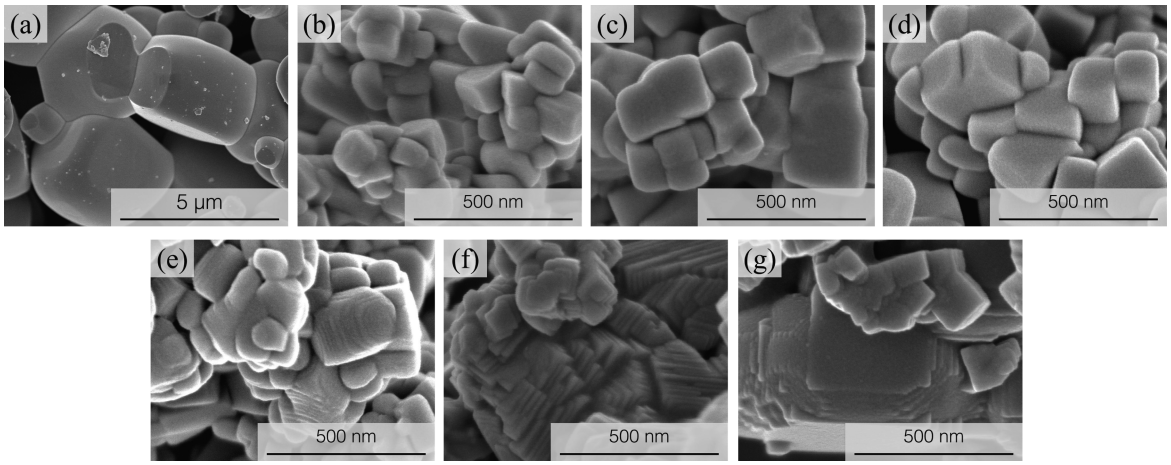

Figure 4. Scanning electron micrographs of Sr-NTO (SSM) doped at a: 0, b: 0.01, c: 0.1, d: 0.3, e: 0.5, f: 0.9, and g: 7.7 mol %.

edge of pristine NTO (SSM) was at 305 nm and shifted to 300 nm upon doping at 0.5 mol %. The edge for the range of 0.5−18.7 mol % stayed at this wavelength and then shifted at 43.5 mol % to a shorter wavelength. $SrSr_{1/3}Ta_{2/3}O_3$ displayed an edge at an even shorter wavelength. The absorption edge wavelength was sensitive to doping at 0−0.5 mol % and insensitive to doping at 0.5−18.7 mol %. The discontinuity at 0.5 mol % suggests that the manner of doping switched from one to the other.

The different types of doping also affected the shape of the photocatalyst particles. Earlier studies[1,2,4] have found that the size and shape of $NaTaO_3$ photocatalyst particles was sensitive to the doping-metal concentration. In the present study, particle shape is plotted as a function of Sr concentration and is related to the different doping types. Figure 4 shows scanning electron micrographs of Sr-NTO (SSM). Pristine NTO (SSM) produced spherical cubes as large as 5 μm in diameter. Doping at 0.01 and 0.1 mol % reduced the particle size to 0.5 μm or smaller, whereas no further contraction occurred at 0.3 mol % or more. At 0.5 mol %, the surfaces of the contracted particles were reconstructed into terraces and steps. There was a threshold concentration for surface reconstruction at 0.5 mol %, which nearly coincided with the threshold for 860 cm^{-1} Raman band generation, that is, the threshold for B-site doping. The terrace width on the reconstructed surface was ∼10 nm and was insensitive to Sr concentration from 0.5 to 7.7 mol %, as seen in the micrographs in Figure 4.

The contracted size and reconstructed surface of Sr-NTO (SSM) particles suggest Sr segregation on the surface. The surface Sr concentration was examined by using XPS. The tantalum 4f emission exhibited doublet peaks of 7/2 and 5/2 spin−orbit couplings, as shown in Figure 5A. The binding energy of each spectrum was calibrated relative to the oxygen 1s level at 530.0 eV to compensate for the charging of X-ray-irradiated semiconductor particles. The binding energy of the 7/2 peak was 25.6 eV, which is consistent with the energy reported for $Sr_2Ta_2O_7$,[27] and displayed the 5+ oxidation state for Ta cations. The spectrum of NTO (SSM) presents broadened peaks, possibly because of inhomogeneous charging on micrometer-sized particles.

The strontium 3d emission presented doublet peaks of 5/2 and 3/2 couplings in Figure 5B. The binding energy of the 5/2 state was 132.6 eV, which is consistent with the 2+ oxidation state.[27] The surface concentration of Sr relative to Ta was estimated from the emission intensity ratio of Sr 3d over Ta 4f. Here, a common escape depth of 2.4 nm was assumed for the Sr 3d and Ta 4f photoelectrons[28] because the kinetic energies of electrons at the two levels were 1.3 and 1.4 keV, respectively, which were nearly equal. The estimated surface concentration is plotted in Figure 5C as a function of the bulk Sr concentration determined via EDX. Surface concentration rapidly increased up to 10 mol % at a bulk concentration of 1.8 mol %, indicating Sr segregation on the surface. The slope of the surface−bulk concentration relation decreased to near unity at bulk concentrations >1.8 mol %. The slope of unity suggests that surface segregation was saturated and that the concentration in the subsurface region accessible by XPS responded to bulk concentration at a one-to-one ratio.

Here, we summarize the results of XRD, Raman scattering, UV−vis absorption, scanning electron microscopy (SEM), and XPS to obtain the picture of Sr-NTO (SSM) in Figure 6. Pristine NTO (SSM) presented spherically cubic particles of micrometer lengths. With Sr doping at <0.3 mol %, Sr^{2+} cations segregated to the particle surface similarly to a surfactant, as illustrated in Figure 6A. The particle size was reduced to accommodate more Sr^{2+} cations. The particle shape simultaneously changed to more cubic, suggesting that the (100) surfaces efficiently accommodated Sr^{2+} cations. The 860 cm^{-1} Raman band was absent at these concentrations, indicating that A sites on the (100) surfaces accommodated the Sr^{2+} cations.

At a threshold concentration of 0.5 mol %, the surface changed, generating regularly separated steps, and the 860 cm^{-1} Raman band appeared simultaneously. The Raman band indicates that B sites of a perovskite-structured tantalate accommodated some Sr cations. To interpret the reconstruction that occurred simultaneously with B-site doping, we propose a Sr-rich $NaTaO_3$−$SrSr_{1/3}Ta_{2/3}O_3$ solid-solution shell formed heteroepitaxially over a $NaTaO_3$ or Sr-poor solid solution core. The steps are generated to release lattice mismatch at the epitaxial interface, as illustrated in Figure 6B. This picture provides a simple interpretation of the regulated step-to-step distances. The Sr-rich solid solution shell requires a step in which lattice mismatch at the core−shell interface exceeds a limit. A one-to-one ratio of the terrace width and step height, which has been observed from a transmission electron micrograph of La-doped $NaTaO_3$,[2] is also easily predicted by the core−shell scheme.

DOI: 10.1021/acscatal.5b00484
ACS Catal. 2015, 5, 3196−3206

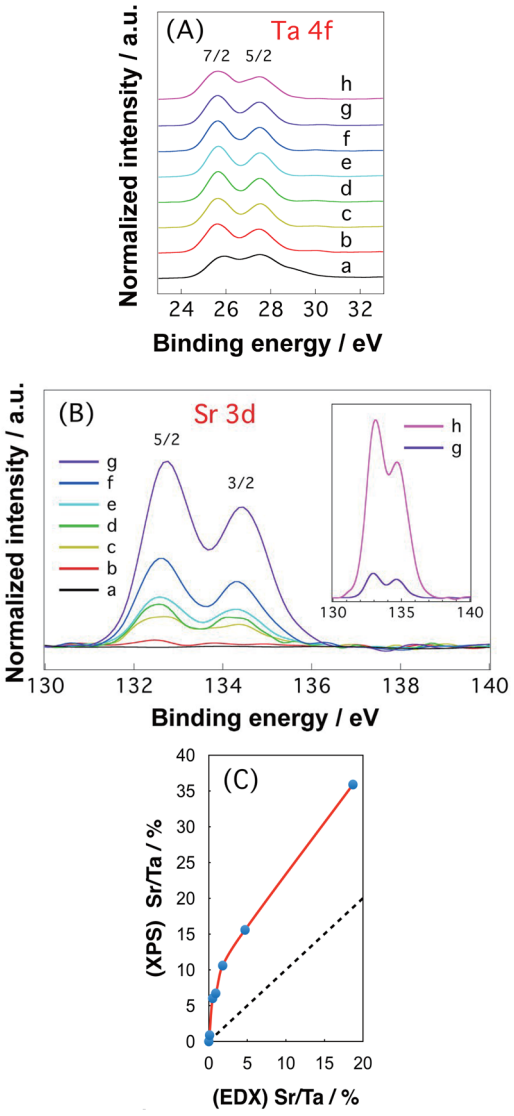

Figure 5. X-ray photoelectron spectra of Sr-NTO (SSM) doped at a, 0; b, 0.1; c, 0.5; d, 0.9; e, 1.8; f, 4.7; and g, 18.7 mol %. The spectrum of $SrSr_{1/3}Ta_{2/3}O_3$ is shown as curve h. In parts A and B, the signal intensity was normalized relative to that of the Ta 4f level. The surface Sr concentration estimated from the XPS results (a–g) is plotted in C as a function of the bulk Sr concentration determined from the EDX results. The broken line represents the relationship with a slope of unity.

Upon Sr doping at more than 0.5 mol %, excess Sr that could not be accommodated in the solid solution shell penetrated the bulk, producing a $NaTaO_3$–$SrSr_{1/3}Ta_{2/3}O_3$ solid-solution core with a corresponding Sr concentration. The number of Sr^{2+} cations in B sites and, hence, the 860 cm^{-1} Raman band intensity increased proportionally to the particle-averaged Sr concentration detected by EDX. The unit cell volume of the solid-solution core also linearly increased with Sr concentration; however, the solid-solution shell included more Sr, and the lattice mismatch was still present at the epitaxial interface, leaving the reconstruction on the surface. The thickness of the Sr-rich shell should be smaller than the escape depth of the Sr 3d and Ta 4f photoelectrons (2.4 nm) because the Sr/Ta molar ratio determined through XPS responded to particle-averaged Sr concentration. On the other hand, the composition of the Sr-rich shell could not be $SrSr_{1/3}Ta_{2/3}O_3$ because the A_{1g} Raman band of surface-reconstructed Sr-NTO (SSM) and $SrSr_{1/3}Ta_{2/3}O_3$ appeared at different wavenumbers (860 and 810 cm^{-1}, respectively).

Surface reconstruction resulting in nanometer-sized steps and terraces on solid solutions of $NaTaO_3$ with $LaIrO_3$,[29] $LaCrO_3$,[30] and $LaFeO_3$[31] were found even though reconstruction mechanisms have not yet been proposed. Step production induced by lattice mismatch at the core–shell interface, which we proposed for Sr-doped $NaTaO_3$, can also be applied to these solid-solution photocatalysts for visible-light harvesting. Solid-solutions of perovskite-structured tantalum oxinirides[32−34] also attract attention in recent years.

Finally, electron–hole recombination in Sr-NTO (SSM) was examined and compared with the intraparticle composition proposed in Figure 6. IR absorption induced by band gap excitation provides a quantitative measure of excited electrons that had not yet recombined. Figures 7A and 7B show the change in IR absorbance of Sr-NTO (SSM) induced by UV light irradiation. Each photocatalyst was fixed on a CaF_2 plate and irradiated with the Hg–Xe lamp in a vacuum. The transmission IR absorption spectrum was obtained in the presence and absence of irradiation by using the Fourier transform spectrometer. To regulate the weight of photocatalyst on the plate, each photocatalyst was suspended in water with a weight concentration of 3 g L^{-1}, and 0.5 mL of the suspension was transferred to the plate and then dried.

UV-induced change in absorbance was positive and increased monotonically from 6000 to 900 cm^{-1}. Absorption of the CaF_2 plate caused a sharp edge at ~900 cm^{-1}. This monotonic IR absorption was observed and assigned to band gap excited electrons in a number of photocatalysts, including $NaTaO_3$,[6]

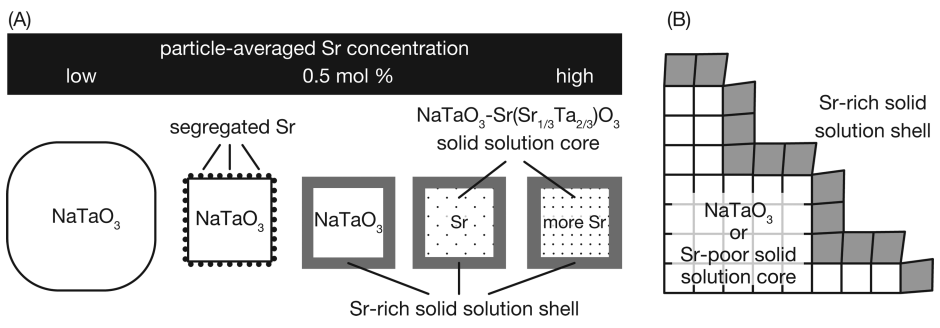

Figure 6. Sr-NTO (SSM) with different Sr concentrations. (A) Cross-sectional composition of particles. (B) Perovskite-structured lattices mismatched at the heteroepitaxial core–shell interface, generating regularly separated steps on the surface. White and gray squares represent unit cells in the core and shell, respectively.

DOI: 10.1021/acscatal.5b00484
ACS Catal. 2015, 5, 3196–3206

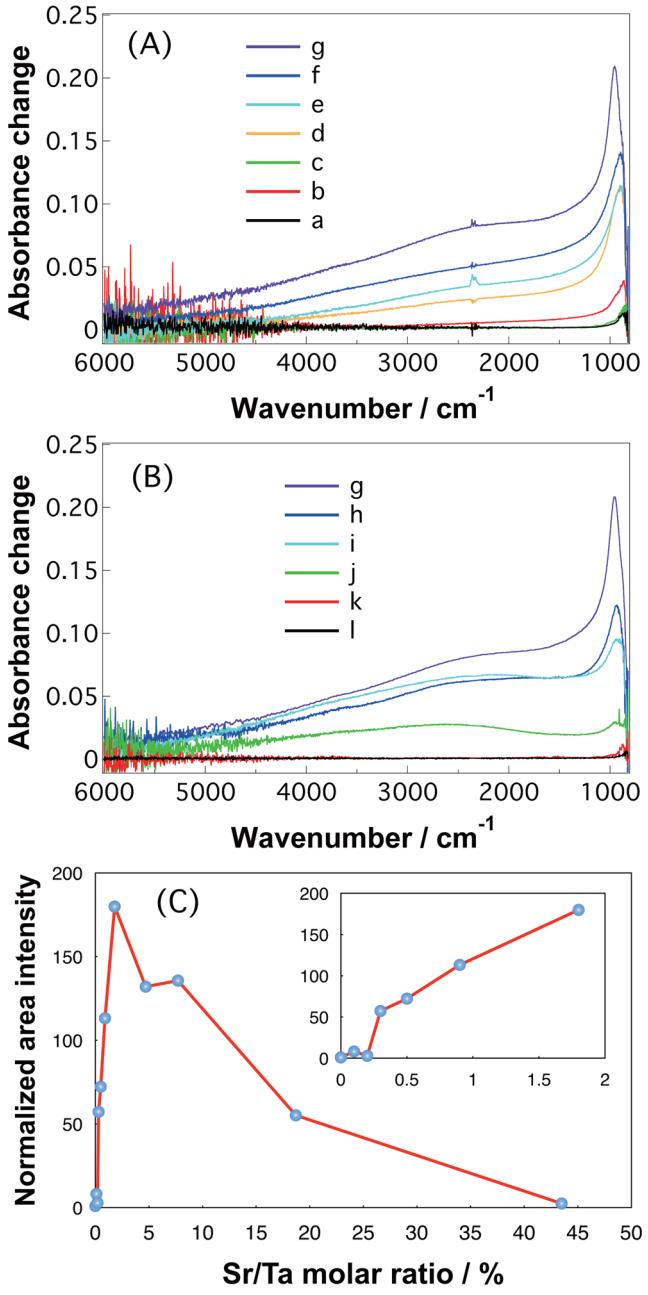

Figure 7. Change in IR absorbance induced by UV light irradiation of Sr-NTO (SSM) doped at a, 0; b, 0.1; c, 0.2; d, 0.3; e, 0.5; f, 0.9; g, 1.8; h, 4.7; i, 7.7; j, 18.7; and k, 43.5 mol %. The spectrum of $SrSr_{1/3}Ta_{2/3}O_3$ is shown as curve l. Integrated absorbance change is plotted in C as a function of Sr concentration. The vertical scale is normalized relative to the integrated absorbance of NTO (SSM).

$SrTiO_3$,[35] and TiO_2.[36−40] Intraband transitions of electrons in the CB, as well as electron transitions from shallow trap states to the CB, are the origins of the IR absorption. Hence, the steady IR absorption indicates a steady population of excited electrons in the irradiated photocatalysts.

Three issues are to be considered here. One is that the absorbance change was enhanced significantly with Sr concentration. Strong responses to a fixed intensity of UV excitation indicate a large electron population and, hence, a restricted electron−hole recombination. Because the photocatalysts were UV-irradiated in a vacuum, the excited electrons in the photocatalyst particles could not be transferred to the

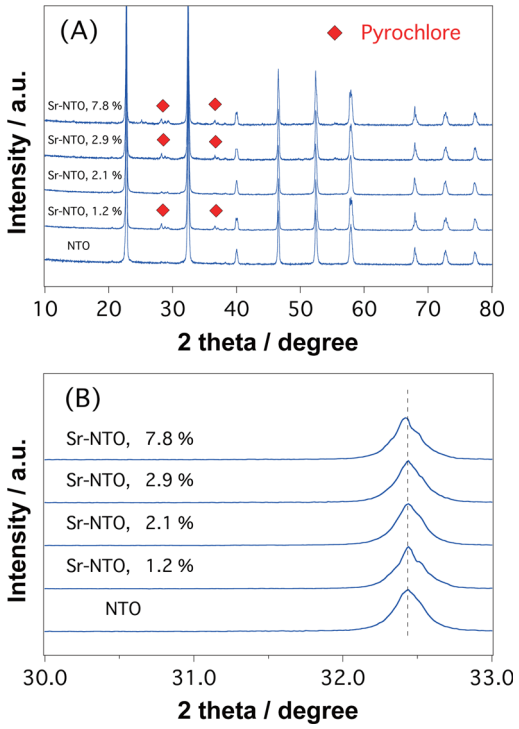

Figure 8. XRD of Sr-NTO (HTM). (A) Whole patterns and (B) shifts of 32° peaks at different Sr concentrations are shown.

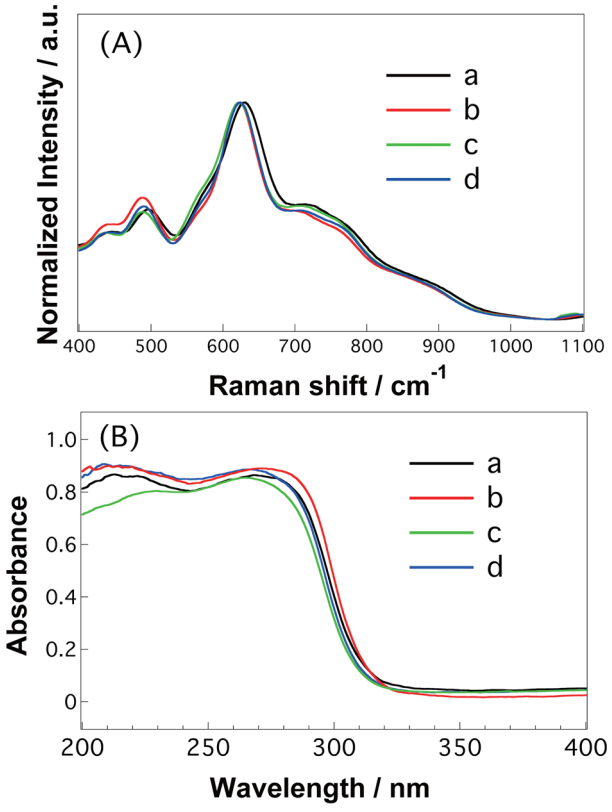

Figure 9. Raman and UV−vis diffuse-reflection spectra of Sr-doped $NaTaO_3$ photocatalysts prepared through HTM using Sr concentrations of a, 0; b, 1.2; c, 2.1; and d, 7.8 mol %. (A) Raman spectra normalized at 620 cm^{-1}. (B) Apparent absorbance of diffuse reflection without Kubelka−Munk transformation.

DOI: 10.1021/acscatal.5b00484
ACS Catal. 2015, 5, 3196−3206

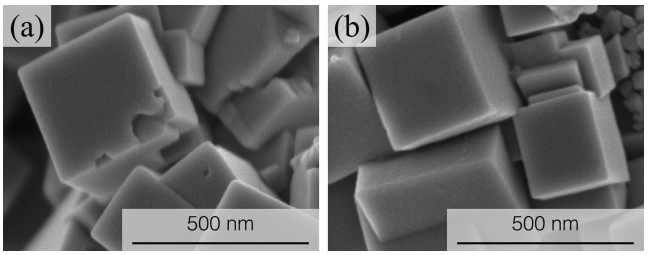

Figure 10. Scanning electron micrographs of Sr-NTO (HTM) doped at a, 0 and b, 2.1 mol %.

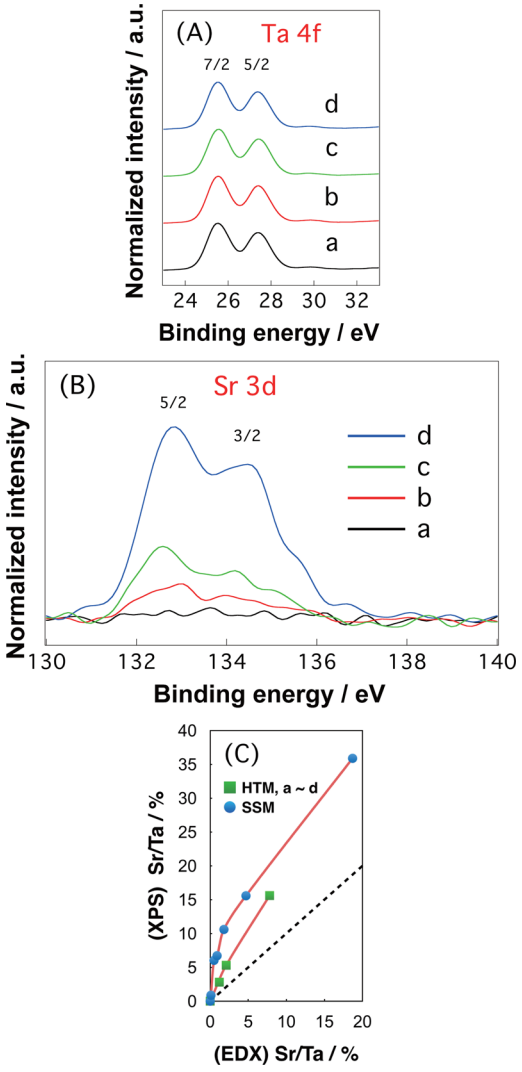

Figure 11. X-ray photoelectron spectra of Sr-NTO (HTM) doped at a, 0; b, 1.2; c, 2.1; and d, 7.8 mol %. In A and B, the signal intensity was normalized relative to that of the Ta 4f level. The surface Sr concentration is plotted in C as a function of bulk Sr concentration, together with the results of SSM-prepared Sr-NTO. The broken line represents the relationship with a slope of unity.

environment. The integrated absorbance change was enhanced by 180 times in Sr-NTO (SSM) doped at 1.8 mol % relative to that of pristine NTO (SSM).[41] The steady population of excited electrons was enhanced by the same extent. The number of electrons is proportional to the integrated absorbance, whereas the absorption cross section per electron is not known. The photodeposition of metallic silver was

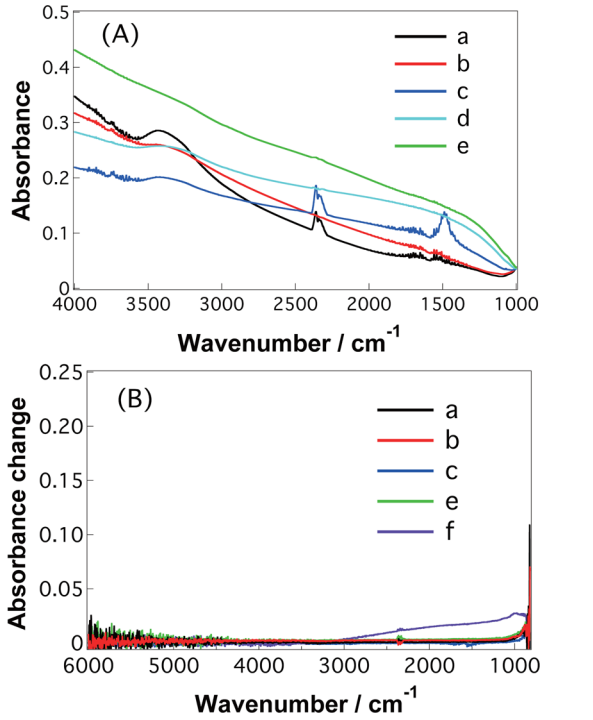

Figure 12. IR absorption spectra of Sr-NTO (HTM). (A) The raw absorbance spectra observed in the absence of UV light irradiation. (B) The change in IR absorbance induced by UV light irradiation. Sr concentrations were a, 0; b, 2.1; and c, 7.8 mol %. The photocatalyst with 2.1% Sr that was dried at 773 and at 1073 K produced curves d and e, respectively. Additional calcination at 1073 K in the presence of $NaCO_3$ produced the absorbance change (curve f).

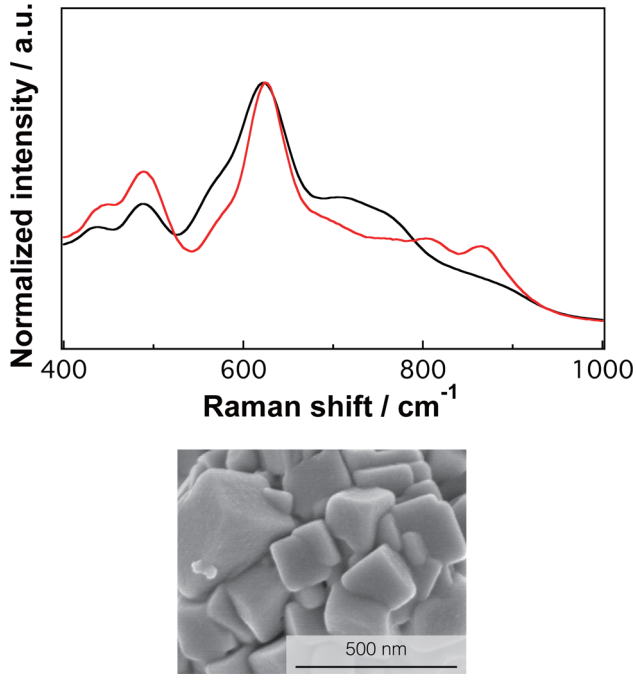

Figure 13. Raman spectrum and SEM image of a Sr-NTO (HTM) dried at 1073 K for 3 h in the presence of $NaCO_3$. The Sr concentration was 2.1 mol %. The Raman spectrum of undried Sr-NTO (HTM) is shown as a black line for reference.

examined by immersing Sr-NTO (SSM) doped at 1.8 mol % in aqueous $AgNO_3$ solution.[42] The observed photodeposition rate

DOI: 10.1021/acscatal.5b00484
ACS Catal. 2015, 5, 3196−3206

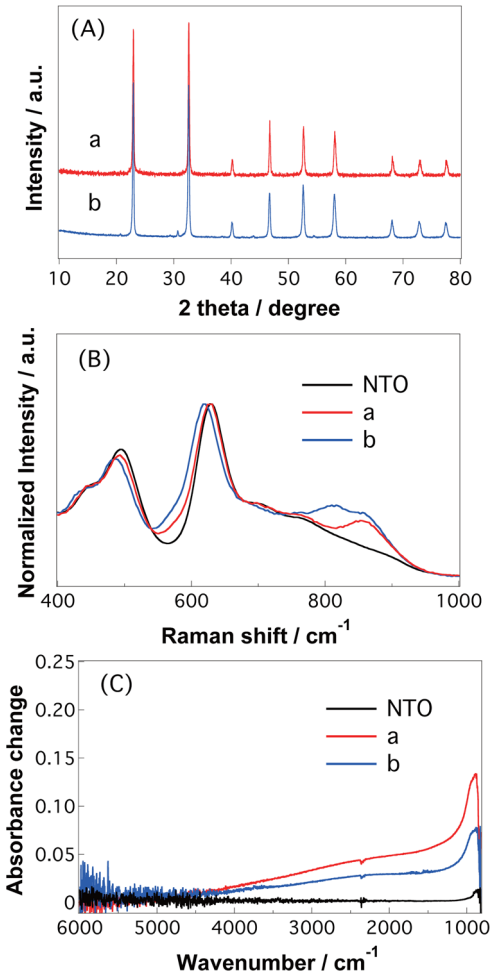

Figure 14. XRD patterns, Raman spectra, and UV-induced IR absorbance changes of (a) Ca-NTO (SSM) and (b) Ba-NTO (SSM). The doping concentrations for Ca and Ba are 4.0 and 5.0 mol %, respectively.

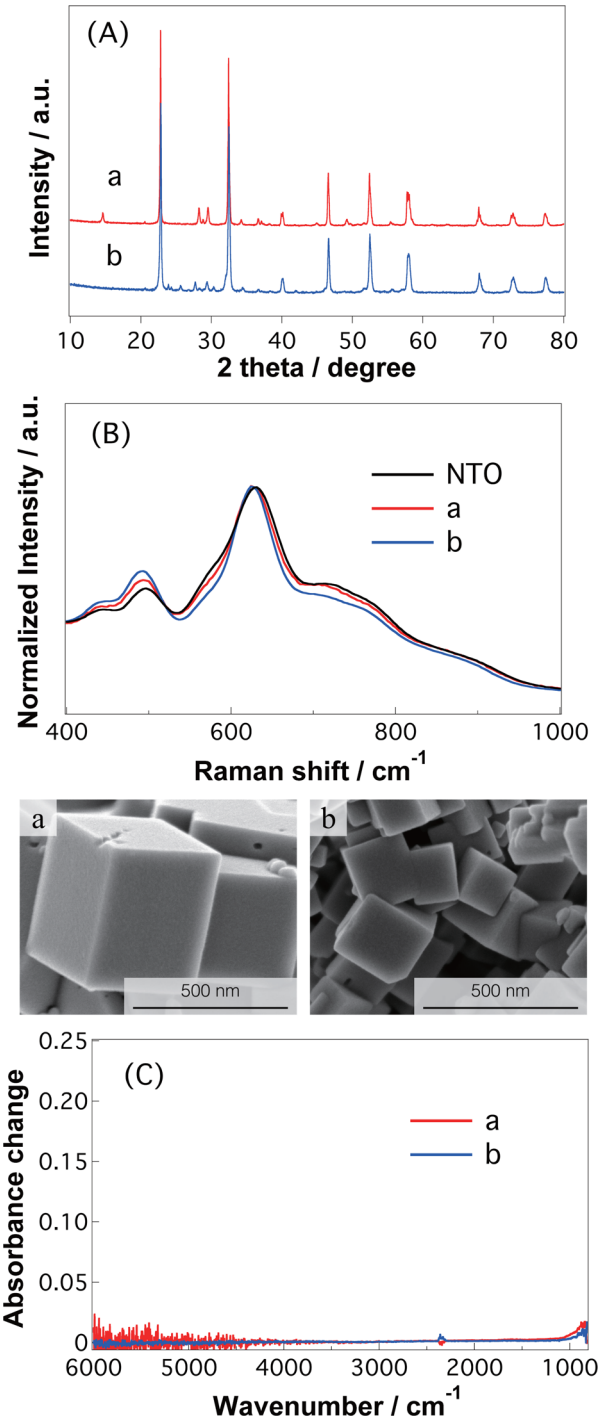

Figure 15. XRD patterns, Raman spectra, SEM images, and UV-induced change in IR absorbance of (a) Ca-NTO (HTM) and (b) Ba-NTO (HTM). The doping concentrations for Ca and Ba were 5.7 and 6.5 mol %, respectively.

was enhanced by five times relative to that exhibited by undoped NTO (SSM). This enhancement was possibly due to restricted electron−hole recombination caused by the doping.

The second issue is a threshold Sr concentration for electron population enhancement. The integrated absorbance at different Sr concentrations is presented in Figure 7C. It increased nearly proportionally to Sr concentration, with a maximum at 1.8 mol %, and then decreased at larger concentrations. Note that there was limited enhancement at 0.1 and 0.2 mol %. Doping at 0.2 mol % caused IR absorption less intense than those at 0.1 and 0.3 mol %. This may result from fluctuation in photocatalyst preparation or IR measurements. A threshold at 0.3 mol % was nearly coincident with the $NaTaO_3$−$SrSr_{1/3}Ta_{2/3}O_3$ solid-solution formation assumed in Figure 6. We therefore propose that Sr doping at B sites was required to restrict electron−hole recombination in $NaTaO_3$. Doping at A sites failed to restrict the recombination. This proposal is further examined and supported with experimental results for HTM-prepared Sr-NTO in Section 3.2.

The electron population was reduced at concentrations above 1.8 mol %. The maximum population at 1.8 mol % suggests electron−hole recombination enhanced by excess Sr^{2+} cations in the solid solution. $SrSr_{1/3}Ta_{2/3}O_3$, the Sr-rich extreme of the solid solution, exhibited no enhancement. These limited or negligible responses are consistent with a reduced H_2 production rate on Sr-NTO (SSM) doped at 8 mol %.[5] Yoshioka et al.[12] reported that $SrSr_{1/3}Ta_{2/3}O_3$ photocatalyst was less active in the water-splitting reaction than were other Sr-containing tantalates ($Sr_2Ta_2O_7$, $Sr_5Ta_4O_{15}$, and $SrTa_2O_6$). The limited activity of $SrSr_{1/3}Ta_{2/3}O_3$ is related to the small electron population observed in this compound. The concentration-dependent mechanisms of restricted *and* enhanced recombination are open for future study. One other aspect related to this

DOI: 10.1021/acscatal.5b00484
ACS Catal. 2015, 5, 3196−3206

issue is the Raman band at 760 cm^{-1}. The strength of this band relative to that of the 860 cm^{-1} band increased at Sr^{2+} concentrations larger than 1.8 mol %. The two A_{1g} bands suggest heterogeneity in Sr-NTO (SSM) with excess Sr^{2+} cations. When this is the case, enhanced recombination may occur in the supposed Sr-rich phase with 760 cm^{-1} band.

The sensitivity of the spectrum shape to Sr concentration is the third issue. The spectrum was monotonic over 0−0.5 mol %. A broad band centered at 2500 cm^{-1} was additionally recognized at larger concentrations. Similar bandlike absorption has been found in time-resolved IR absorption spectra of UV-irradiated La-doped $NaTaO_3$ at the same wavenumber region[6] and in spectra of visible-light-irradiated $LaTiO_2N$ at 6000 cm^{-1}.[43] These bandlike absorptions are attributed to electron transitions from midgap states to the CB. The energy depth of the midgap states relative to the CB bottom is estimated from the absorption wavenumber, which is 0.3 eV for the center wavenumber of Sr-NTO (SSM) observed in the present study. A detectable fraction of band gap excited electrons were quickly trapped in the midgap states and then re-excited to the CB by absorption of IR light. This interpretation suggests that Sr doping created midgap states in $NaTaO_3$. The relationship between the midgap states and restricted recombination is an interesting topic for future study.

3.2. Sr-NTO (HTM). Strontium-doped $NaTaO_3$ photocatalysts were prepared by HTM using Sr concentrations of 0, 1.2, 2.1, 2.9, and 7.8 mol %. In XRD, the diffraction peaks of the perovskite phase were dominant, as shown in Figure 8A. Minor contributions from a pyrochlore phase were also recognized. In hydrothermal synthesis of $KTaO_3$,[44] a defect pyrochlore, $KTa_2O_5(OH)$, appeared as an intermediate phase that converted to the perovskite product. A Na-containing pyrochlore could be the minor phase that was recognized in the present study. In Sr-NTO (SSM), the diffraction peaks broadened and shifted to lower angles with increasing Sr concentration. On the other hand, those of Sr-NTO (HTM) displayed no broadening or shifting, as depicted in Figure 8B. The diffraction angle that was insensitive to Sr concentration suggests the absence of $NaTaO_3$−$SrSr_{1/3}Ta_{2/3}O_3$ solid solutions in Sr-NTO (HTM).

Raman scattering provided evidence for the absence of the solid solution. The Raman band at 860 cm^{-1}, which is attributable to B-site-doped $NaTaO_3$, is absent in the Sr-NTO (HTM) spectra, as shown in Figure 9A. We thus assume that the Sr^{2+} cations selectively occupied A sites during HTM using any of the examined Sr concentrations. Cation exchange at the A sites did not induce the A_{1g} Raman band, as was confirmed with K-NTO in Section 3.1.

Doping metal occupancies at the A sites or B sites in $NaTaO_3$ doped with Bi,[45] Cr,[46] or Eu,[47] were examined and were found to be sensitive to the Na/Ta molar ratio; however, these conclusions were supported mainly by lattice parameters determined from XRD. Our study suggests that Raman spectroscopy provides a direct and sensitive measure of B-site doping in $NaTaO_3$ photocatalysts.

UV−vis diffuse-reflection spectra of Sr-NTO (HTM), which are presented in Figure 9B, were insensitive to Sr doping. The short-wavelength shift of the absorption edge was unrecognizable. This is consistent with A-site doping, since atomic orbitals of the A-site cations contribute little to the CB and the valence band. All bulk-sensitive characterization results obtained from XRD, Raman, and UV−vis spectroscopy indicate that the perovskite lattice of $NaTaO_3$ was modified with selective doping of A sites through HTM.

SEM images (Figure 10) show that Sr-NTO (HTM) exhibited perfect cubes with no sign of surface reconstruction. The cube length was within 0.2−0.5 μm and remained insensitive to Sr concentration. These features have a clear contrast to what was observed with Sr-NTO (SSM). A limited number of small, irregularly shaped particles appeared in addition to the cubes. These small particles might be of the pyrochlore recognized from XRD.

Figures 11A and 11B show XPS spectra of Sr-NTO (HTM). The Ta 4f spectra are identical to those observed for photocatalysts prepared through SSM and indicate the 5+ oxidation state of Ta cations. The binding energy of the Sr 3d peaks is consistent with the 2+ oxidation state of this metal element. The broader peaks suggest heterogeneous environments of Sr^{2+} cations probably affected by water-derived species residing in the hydrothermally prepared crystals. Sr-NTO (HTM) included water-derived species, as described in the following paragraphs. The Sr/Ta molar ratio at the surface, which was estimated from the XPS signal intensities, was larger than the particle-averaged concentration by a factor of 2, in Figure 11C. Strontium segregation on the surface was thus evident. On the other hand, the surface concentration was nearly proportional to the particle-averaged concentration. The surface concentration on Sr-NTO (SSM) increased rapidly at low particle-averaged concentrations and then increased moderately at higher concentrations. The core−shell solid solutions caused initial rapid increases, followed by moderate responses. The more proportional responses observed with Sr-NTO (HTM) are consistent with the absence of core−shell structures.

Photocatalyst particles that crystallize in HTM are always in contact with an aqueous solution, whereas they are in contact with air in SSM. The surface energy of a solid in vapor is often large and is lower in solutions. The thermodynamics and kinetics of Sr-NTO crystallization would thus be more sensitive to surface properties in SSM and would be less sensitive in HTM. This may explain why SSM produces core−shell structures, whereas HTM does not.

$KTaO_3$ prepared through HTM contains finite amounts of OH^- and H_2O.[44] This was also the case with Sr-NTO (HTM). A broad IR absorption band corresponding to water-derived species appeared at 3000−3600 cm^{-1} in the spectra of two kinds of Sr-NTO (HTM), as shown in Figure 12A. Figure 12B presents the change in IR absorbance induced by UV light irradiation. Pristine NTO (HTM) produced a weak response with a monotonic absorbance-change spectrum similar to that observed with NTO (SSM). The monotonic spectrum is attributed to the optical transitions of band gap excited electrons. Because of doping with Sr at 2.1 and even at 7.8 mol %, the change in UV-induced absorbance remained small. Weak responses to UV light irradiation indicate that excited electrons efficiently recombined with holes. Strontium doping at A sites alone failed to restrict electron−hole recombination. This observation is compatible with the absence of an increase in electron population in Sr-NTO (SSM) at Sr concentrations below 0.3 mol %, at which A sites were selectively doped.

Li and Zhang[10] prepared $NaTaO_3$ doped with La at 0−5 mol % by HTM and obtained cubic particles similar to those of Sr-NTO (HTM). They examined photocatalytic dye decomposition and observed a maximum decomposition rate at a La concentration of 2 mol %. However, the maximum rate

DOI: 10.1021/acscatal.5b00484
ACS Catal. 2015, 5, 3196−3206

enhancement was still a 20% increase relative to the rate with nondoped $NaTaO_3$. This number is much smaller than that of the rate enhancement for water splitting observed with metal-doped $NaTaO_3$ prepared via SSM.[1,2,4,5] The limited enhancement of the reaction rate with La-doped $NaTaO_3$ prepared through HTM might result from the limited increase in electron population caused by A-site doping. Our present study demonstrates that the two preparation methods produced two different compounds.

The water-derived species residing in the photocatalysts prepared through HTM might be the cause of the efficient recombination. To examine and exclude this interpretation, Sr-NTO (HTM) doped at 2.1 mol % was dried at elevated temperatures in air. Heating at 1073 K for 3 h eliminated the IR absorption of water-derived species, as shown by curve e in Figure 12A, but the absorption remained at 773 K (curve d). Curve e of Figure 12B shows that 1073-K-dried photocatalyst exhibited a weak response to UV irradiation. An additional 3 h of calcination in the presence of $NaCO_3$ at 1073 K was performed to restore Na cation vacancies, if any, produced by the evacuation of water-derived species. The UV-induced absorbance change of the sample with restored Na was still weaker than that of Sr-NTO (SSM), as shown by curve f in Figure 12B. Hence, the water-derived species played a limited role in electron−hole recombination in HTM-prepared photocatalysts.

The Raman spectrum and SEM image of the sample with restored Na are shown in Figure 13. The marker band at 860 cm^{-1} appears to indicate the relocation of some Sr^{2+} cations from A sites to B sites. This temperature-induced relocation suggests that Sr doping at A sites alone is thermodynamically less stable in $NaTaO_3$ than solid-solution formation with $SrSr_{1/3}Ta_{2/3}O_3$. This further suggests that A-site doping with HTM is kinetically favorable. Surface reconstruction, which generates nanometer-scale steps, was absent in the sample with restored Na.

3.3. Ca- or Ba-NTO. $NaTaO_3$ photocatalysts doped with Ca or Ba were prepared through SSM and HTM for comparison with Sr-NTO. Figure 14 shows the XRD, Raman, and IR absorption results for Ca-NTO (SSM) and Ba-NTO (SSM). The doping concentrations for Ca and Ba were 4.0 and 5.0 mol %, respectively. The XRD patterns in Figure 14A indicate a single perovskite phase for the doped photocatalysts. An additional Raman band appeared at 860 cm^{-1} in Figure 14B. Doping with the three alkaline-earth metals (Sr, Ca, and Ba) always produced a band at 860 cm^{-1}. The common wavenumber for the different doping metals is attributed to TaO_6 breathing vibration in B-site-doped M-NTO. In Figure 14C, the IR absorbance increased upon irradiation with UV light. The spectrum of absorbance change was monotonic, being similar to that of Sr-NTO. This similarity is attributed to the absorption of band gap excited electrons. The integrated absorbance for Ca-NTO and Ba-NTO was enhanced 91 and 62 times, respectively.

Doping through HTM was further examined. The doping concentrations for Ca and Ba were 5.7 and 6.5 mol %, respectively. The XRD patterns shown in Figure 15A include a dominant contribution from perovskite-structured M-NTO with a limited contribution from pyrochlore phases. Peak broadening or low-angle shift is not apparent. The 860 cm^{-1} Raman band was not produced by Ca-NTO (HTM) and Ba-NTO (HTM) in Figure 15B. Scanning electron micrographs show perfect cubes of 0.2−0.5 μm in length with no sign of surface reconstruction. These features are fully compatible with the results for Sr-NTO (HTM) and demonstrate A-site doping of Ca-NTO (HTM) and Ba-NTO (HTM). Figure 15C shows the UV-induced IR absorbance change of the two photocatalysts. The response to UV irradiation remained weak, as expected. Thus, A-site doping of Ca or Ba failed to restrict electron−hole recombination in $NaTaO_3$.

4. CONCLUSION

Solid-state and hydrothermal syntheses produced Sr-doped $NaTaO_3$ photocatalysts with the same chemical formula but different chemical structures. Because of SSM, (100) surfaces of the cubic particles accommodated Sr^{2+} cations in the A sites of the perovskite-structured lattice at Sr concentrations below 0.3 mol %. By doping more than 0.5 mol %, Sr^{2+} cations occupied both A and B sites to produce core−shell structures of $NaTaO_3$−$SrSr_{1/3}Ta_{2/3}O_3$ solid solutions. A Sr-rich shell covered a Sr-poor core. The lattice mismatch at the heteroepitaxial core−shell interface induced surface reconstruction with regularly separated nanometer-scale steps. Electron−hole recombination was restricted in the solid-solution photocatalysts. The steady-state population of electrons excited with the Hg−Xe lamp was enhanced by 180 times at a Sr concentration of 1.8 mol %. With HTM, Sr^{2+} cations were in A sites alone, providing no surface reconstruction and no electron population enhancement. Compatible results were obtained with doping with Ca or Ba instead of Sr. The choice of element was not the only factor determining the success of metal doping; tuning of doping sites was essential to restricting the recombination in $NaTaO_3$ photocatalysts. Postsynthetic drying of hydrothermally prepared photocatalysts resulted in a limited increase in the electron population accompanied by partial relocation of Sr^{2+} cations from A sites to B sites.

AUTHOR INFORMATION

Corresponding Author

*E-mail: oni@kobe-u.ac.jp.

Notes

The authors declare no competing financial interest.

ACKNOWLEDGMENTS

Hidenori Saito of Kanagawa Academy of Science and Technology operated the scanning electron microscope. Akihide Wada of Kobe University guided L.A. in observing the Raman spectra. This study was financially supported by the Nippon Sheet Glass Foundation for Materials Science and Engineering and by a Grant-in-Aid (No. 24655014 and 26630411) for Exploratory Research.

REFERENCES

(1) Kudo, A.; Kato, H. *Chem. Phys. Lett.* **2000**, *331*, 373−377.
(2) Kato, H.; Asakura, K.; Kudo, A. *J. Am. Chem. Soc.* **2003**, *125*, 3082−3089.
(3) Sakata, Y.; Matsuda, Y.; Yanagida, T.; Hirata, K.; Imamura, H.; Teramura, K. *Catal. Lett.* **2008**, *125*, 22−26.
(4) Iwase, A.; Kato, H.; Okutomi, H.; Kudo, A. *Chem. Lett.* **2004**, *33*, 1260−1261.
(5) Iwase, A.; Kato, H.; Kudo, A. *ChemSusChem* **2009**, *2*, 873−877.
(6) Yamakata, A.; Ishibashi, T.; Kato, H.; Kudo, A.; Onishi, H. *J. Phys. Chem. B* **2003**, *107*, 14383−14387.
(7) Maruyama, M.; Iwase, A.; Kato, H.; Kudo, A.; Onishi, H. *J. Phys. Chem. C* **2009**, *113*, 13918−13923.

DOI: 10.1021/acscatal.5b00484
ACS Catal. 2015, 5, 3196−3206

(8) He, Y.; Zhu, Y.; Wu, N. *J. Solid State Chem.* **2004**, *177*, 3868−3872.
(9) Lee, Y.; Watanabe, T.; Takata, T.; Hara, M.; Yoshimura, M.; Domen, K. *Bull. Chem. Soc. Jpn.* **2007**, *80*, 423−428.
(10) Li, X.; Zang, J. *Catal. Commun.* **2011**, *12*, 1380−1383.
(11) Ahtee, M.; Unonius, L. *Acta Crystallogr., Sect. A: Cryst. Phys., Diffr., Theor. Gen. Crystallogr.* **1977**, *33*, 150−154.
(12) Yoshioka, K.; Petrykin, V.; Kakihana, M.; Kato, H.; Kudo, A. *J. Catal.* **2005**, *232*, 102−107.
(13) Caldes, M. T.; Deniard, P.; Zou, X. D.; Marchand, R.; Diot, N.; Brec, R. *Micron* **2001**, *32*, 497−507.
(14) Shannon, R. D. *Acta Crystallogr., Sect. A: Cryst. Phys., Diffr., Theor. Gen. Crystallogr.* **1976**, *32*, 751−767.
(15) Shimura, K.; Kato, S.; Yoshida, T.; Itoh, H.; Hattori, T.; Yoshida, H. *J. Phys. Chem. C* **2010**, *114*, 3493−3503.
(16) Sun, J.; Chen, G.; Pei, J.; Jin, R.; Wang, Q.; Guang, X. *J. Mater. Chem.* **2012**, *22*, 5609−5614.
(17) Teixeira, N. G.; Dias, A.; Moreira, R. L. *J. Eur. Ceram. Soc.* **2007**, *27*, 3683−3686.
(18) Siny, I. G.; Tao, R.; Katiyar, R. S.; Guo, R.; Bhalla, A. S. *J. Phys. Chem. Solids* **1998**, *59*, 181−195.
(19) Zheng, H.; Reaney, I. M.; Csete de Györgyfalva, G. D. C.; Ubic, R.; Yarwood, J.; Seabra, M. P.; Ferreira, V. M. *J. Mater. Res.* **2004**, *19*, 488−495.
(20) Smolensky, G. A.; Siny, I. G.; Pisarev, R. V.; Kuzminov, E. G. *Ferroelectrics* **1976**, *12*, 135−136.
(21) Perry, C. H.; Tornberg, N. E. *Phys. Rev.* **1969**, *183*, 595−603.
(22) Hu, C.-C.; Lee, Y.-L.; Teng, H. *J. Mater. Chem.* **2011**, *21*, 3824−3830.
(23) Sun, J.; Chen, G.; Li, Y.; Jin, R.; Wang, Q.; Pei, J. *Energy Environ. Sci.* **2011**, *4*, 4052−4060.
(24) Choi, M.; Oba, F.; Tanaka, I. *Phys. Rev. B: Condens. Matter Mater. Phys.* **2008**, *78*, 014115 (8 pages) .
(25) Kato, H.; Kobayashi, H.; Kudo, A. *J. Phys. Chem. B* **2002**, *106*, 12441−12447.
(26) Wang, H.; Wu, F.; Jiang, H. *J. Phys. Chem. C* **2011**, *115*, 16180−16186.
(27) Atuchin, V. V.; Grivel, J.-C.; Zhang, Z. *Chem. Phys.* **2009**, *360*, 74−78.
(28) Ertl, G.; Küppers, J. *Low Energy Electrons and Surface Chemistry*; Wiley-VCH Verlag: Weinheim, 1986; p 7.
(29) Iwase, A.; Saito, K.; Kudo, A. *Bull. Chem. Soc. Jpn.* **2009**, *82*, 514−518.
(30) Yi, Z.-G.; Ye, J.-H. *J. Appl. Phys.* **2009**, *106*, 074910.
(31) Kanhere, P.; Nisar, J.; Tang, Y.; Pathak, B.; Ahuja, R.; Zheng, J.; Chen, Z. *J. Phys. Chem. C* **2012**, *116*, 22767−22773.
(32) Ueda, K.; Kato, H.; Kobayashi, M.; Hara, M.; Kakihana, M. *J. Mater. Chem. A* **2013**, *1*, 3667−3674.
(33) Maeda, K.; Lu, D.; Domen, K. *ACS Catal.* **2013**, *3*, 1026−1033.
(34) Modak, K.; Srinivasu, K.; Ghosh, K. *J. Phys. Chem. C* **2014**, *118*, 10711−10719.
(35) Furuhashi, K.; Qingxin, J.; Kudo, A.; Onishi, H. *J. Phys. Chem. C* **2013**, *117*, 19101−19106.
(36) Yamakata, A.; Ishibashi, T.; Onishi, H. *Chem. Phys. Lett.* **2001**, *333*, 271−277.
(37) Szczepankiewicz, S. H.; Moss, J. A.; Hoffmann, M. R. *J. Phys. Chem. B* **2002**, *106*, 2922−2927.
(38) Yoshihara, T.; Katoh, R.; Furube, A.; Tamaki, Y.; Murai, M.; Hara, K.; Murata, S.; Arakawa, H.; Tachiya, M. *J. Phys. Chem. B* **2004**, *108*, 3817−3823.
(39) Warren, D. S.; McQuillan, A. J. *J. Phys. Chem. B* **2004**, *108*, 19373−19379.
(40) Panayotov, D. A.; Burrows, S. P.; Morris, J. R. *J. Phys. Chem. C* **2012**, *116*, 4535−4544.
(41) Absorbance change of curves a−c was integrated in a range of 820−2000 cm^{-1} to avoid contribution of noize at high wavenumbers. Absorbance change of the other curves was accumulated in the full range of 820−6000 cm^{-1}.
(42) An, L.; Onishi, H. *e-J. Surf. Sci. Nanotechnol.* **2015**, in press.
(43) Yamakata, A.; Kawaguchi, M.; Nishimura, N.; Minegishi, T.; Kubota, J.; Domen, K. *J. Phys. Chem. C* **2014**, *118*, 23897−23906.
(44) Goh, G. K. L.; Haile, S. M.; Levi, C. G.; Lange, F. F. *J. Mater. Res.* **2002**, *17*, 3168−3176.
(45) Kanhere, P. D.; Zheng, J.; Chen, Z. *J. Phys. Chem. C* **2011**, *115*, 11846−11853.
(46) Su, Y.; Wang, S.; Meng, Y.; Han, H.; Wang, X. *RSC Adv.* **2012**, *2*, 12932−12939.
(47) Su, Y.; Peng, L.; Guo, J.; Huang, S.; Lv, L.; Wang, X. *J. Phys. Chem. C* **2014**, *118*, 10728−10739.

DOI: 10.1021/acscatal.5b00484
ACS Catal. 2015, 5, 3196−3206